Research Article

Nano Research
2020, 13(7): 1982–1987

ISSN 1998-0124 CN 11-5974/O4
https://doi.org/10.1007/s12274-020-2895-5

Local modulation of excitons and trions in monolayer WS_2 by carbon nanotubes

Rui Feng[1,2], Shicheng Xu[1], Weiming Liu[1], Peng Gao[3], Jin Zhang[1] (✉), and Lianming Tong[1] (✉)

[1] *Center for Nanochemistry, Beijing Science and Engineering Center for Nanocarbons, Beijing National Laboratory for Molecular Sciences, College of Chemistry and Molecular Engineering, Peking University, Beijing 100871, China*
[2] *Academy for Advanced Interdisciplinary Studies, Peking University, Beijing 100871, China*
[3] *School of Physics, Peking University, Beijing 100871, China*

Received: 12 February 2020 / **Revised:** 19 May 2020 / **Accepted:** 21 May 2020

ABSTRACT

Mixed dimensional van der Waals (vdW) heterostructures constructed by one-dimensional (1D) and two-dimensional (2D) materials exhibit extra degree of freedom to modulate the electronic and optical properties due to the combination of different dimensionalities. The charge transfer at the interface between 1D and 2D materials plays a crucial role in the optoelectronic properties and performance of the heterostructure-based devices. Here, we stacked single-walled carbon nanotubes (SWNTs) on monolayer WS_2 for a mixed dimensional vdW heterostructure, and investigated the local modulation of excitons and trions in WS_2 by SWNTs. Different directions of charge transfer between SWNTs and WS_2 are evidenced by the photoluminescence (PL) spectra of WS_2. The PL intensity can be either enhanced or weakened by individual SWNTs. In our work, the PL intensity of WS_2 is enhanced and the exciton peak position heterostructure is red-shifted about 3 meV due to the charge transfer from WS_2 to an individual SWNT (SWNT#1). The change of PL by another SWNT (SWNT#2) can not be well-resolved in far-field, but scanning near-field optical microscope (SNOM) measurements show that the PL intensity of WS_2 is weakened by the SWNT. The peak position of exciton is blue-shifted by ~ 1 meV while that of trion is redshifted by ~ 1 meV due to the charge transfer from the SWNT to WS_2. These results give insight into the charge transfer at the interface of SWNT/WS_2 heterostructure, and can be useful for design of optoelectronic devices based on mixed dimensional vdW heterostructures.

KEYWORDS

WS_2, single-walled carbon nanotube (SWNT), mixed dimensional heterostructure, excitons, trion

1 Introduction

Two-dimensional (2D) transition metal dichalcogenides (TMDs) materials have been a wide platform for designing future optical and optoelectronic devices with unprecedented performance, such as light-emitting diodes, photodetectors and solar cells [1–4]. By stacking two different 2D materials together, van der Waals (vdW) heterostructures can be constructed and have opened possibilities for new physics and novel applications. In recent years, mixed dimensional vdW heterostructures, that is, vdW heterostructures constructed by 2D materials and zero- (0D), one- (1D) or three- (3D) dimensional materials, have emerged and provided a new degree of freedom to engineer their physical properties and device performance [5]. For example, Wu et al. demonstrated that photodetector made from $CsPbI_{3-x}Br_x$ perovskite quantum dots (0D) and monolayer MoS_2 (2D) has extremely high photoresponsivity of 7.7×10^4 A·W^{-1} which is superior to 2D vdW heterostructures [6]. In addition, 1D/2D vdW heterostructures inherit properties of both directionality from 1D and planarity from 2D materials [1, 7, 8]. Qin et al. demonstrated that phototransistor consisting of heterostructures based on trigonal selenium (t-Se) nanobelt and few layer-ReS_2 has showed enhanced responsivity and detectivity up to 98 A·W^{-1} and 6×10^{10} Jones with reduced response time compared with bare ReS_2 [9]. Henning et al. reported that heterojunction diodes consisting of Si nanowire and MoS_2 showed an instrument-limited response time of 1 μs, ten times faster than that for previously reported planer Si/MoS_2 heterojunctions [10].

Among the 1D materials, single-walled carbon nanotubes (SWNTs) have attracted great interest in both scientific research and industrial applications [11]. The electronic band structure of a SWNT is determined by the chiral index (n, m). If $(n - m)/3$ is an integer, it is metallic, and otherwise semiconducting. The size of band gap of SWNTs can range from infrared to ultraviolet, which is suitable for a variety of applications combined with 2D materials [12–14]. For example, it has been reported that SWNT/MoS_2 heterostructure can be used for microwave-absorbing with a maximum effective absorption bandwidth of 5.60 GHz, much higher than other MoS_2-based heterostructures [7]. Recently, a method of controlled sequential chemical vapor deposition (CVD) growth was developed to grow strongly coupled heterostructures of monolayer MoS_2 and carbon nanotubes [15]. However, the charge transfer at the 1D/2D interface and the influence to the excitons and trions of TMDs materials have not been well studied yet.

In this work, we investigated the excitonic behavior at the interface of SWNT/WS_2 mixed dimensional vdW heterostructure

Address correspondence to Jin Zhang, jinzhang@pku.edu.cn; Lianming Tong, tonglm@pku.edu.cn

through photoluminescence (PL) spectra. Different modulation of excitons and trions in WS_2 was observed for different individual SWNTs. For a heterostructure constructed by SWNT#1 (metallic type) and WS_2, the exciton PL peak of WS_2 was red-shifted, while the total intensity was enhanced compared with that of monolayer WS_2 without SWNT. In another heterostructure constructed by SWNT#2 (semiconducting type) and WS_2, the change of PL can not be well-resolved in far-field, but can be observed by scanning near-field optical microscope (SNOM). The peak position of exciton was blue-shifted while that of trion was red-shifted, and the total intensity was weakened. The decrease of intensity ratio between trions and excitons $\frac{I_{A^-}}{I_A}$ for the SWNT#1/WS_2 heterostructure implies that the charge transfer occurs from WS_2 to the SWNT. On the other hand, the increase of $\frac{I_{A^-}}{I_A}$ for the SWNT#2/WS_2 heterostructure indicates that the charge transfer occurs from the SWNT to WS_2. The excitation power dependence of the PL spectra further confirmed the different charge transfer processes. The findings of the local modulation of excitonic features can inspire the development of optoelectronics based on 1D/2D mixed dimensional vdW heterostructures.

2 Experimental

2.1 Growth of horizontally aligned SWNTs arrays on quartz substrates

Stable temperature cut (ST-cut) quartz substrates (single-side polished, miscut angle < 0.5°, surface roughness < 5 Å) underwent a necessary annealing process at 900 °C in air for 8 h. Then 0.05 mmol/L $Fe(OH)_3$/ ethanol solution was dispersed onto the substrates by the spin-coating method. The quartz substrates with well-dispersed iron species were placed into a 1-inch tube and heated to the desired temperature (~ 850 °C) within 40 min in air. After that, 300 standard cubic centimeters per minute (sccm) argon, 200 sccm hydrogen and 50 sccm argon through an ethanol bubbler were introduced into the system for the synthesis of horizontally aligned SWNTs with a suitable density on quartz substrates. After 30 min growth, the SWNT samples were cooled down to ambient temperature under the protection of argon.

2.2 Transfer process

The SWNTs arrays were transferred to a 0.2 mm thick transparent quartz glass using polymethylmethacrylate (PMMA). Monolayer WS_2 was obtained by mechanical exfoliation and transferred to the top of the carbon nanotube arrays.

2.3 Optical measurements

Far-field PL and Raman spectroscopy were performed using a WITec alpha300 system with an excitation wavelength of 488 nm and spatial resolution of ~ 330 nm with a 100× objective (NA = 0.9). The excitation power for Raman measurements was controlled between 300 μW to 400 μW. The excitation power for PL varied from 1 μW to 200 μW to investigate the influence of charge transfer under different optical doping levels. The near-field PL spectroscopy was performed using an aperture AFM probe on WITec alpha 300 and the size of aperture was about 150 nm.

3 Results and discussion

Figure 1(a) shows the schematic of SWNT/WS_2 mixed dimensional vdW heterostructure. Monolayer WS_2 was mechanically exfoliated on PMMA. The density of the SWNTs array was controlled to be less than 2 tubes/μm. The SWNTs array was first transferred onto a transparent quartz substrate. Then a monolayer WS_2 was site-specifically transferred onto the SWNTs array. Figures 1(b) and 1(c) show the optical image and scanning electron microscope (SEM) image of a monolayer WS_2 covered on an array of SWNTs, respectively. The bright stripe at the right side of WS_2 corresponds to multilayers. Raman mapping excited by 488 nm laser was performed, and the mapping image of the G peak (1,592 cm^{-1}) of SWNTs was plotted in Fig. 1(d). It is clear that only a few nanotubes on resonance with the excitation laser were seen in the Raman mapping image. The appearance of the signal from WS_2 was due to the PL of the B exciton (~ 530 nm) [16]. The Raman spectra obtained from different spots marked in Fig. 1(c) were shown in Fig. 1(e), that is, on WS_2 (blue curve), on a selected SWNT (SWNT#1, black curve), and on the SWNT/WS_2

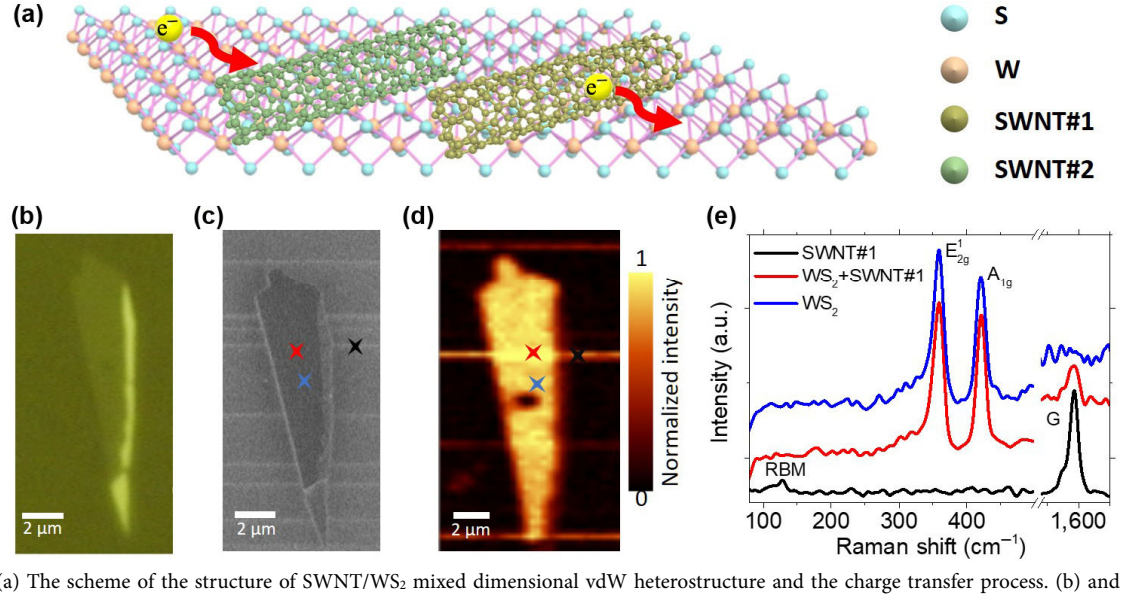

Figure 1 (a) The scheme of the structure of SWNT/WS_2 mixed dimensional vdW heterostructure and the charge transfer process. (b) and (c) Optical microscope (OM) and SEM images of SWNT/WS_2 mixed-dimensional heterostructures. (d) The Raman mapping of the G peak of SWNT at 1,592 cm^{-1}. (e) The Raman spectra chosen from three sites marked in (d) as red, blue and black which represent SWNT/WS_2, WS_2 and SWNT.

heterostructure (red curve). From the Raman spectrum of WS_2, the in-plane mode E^1_{2g} and out-of-plane mode A_{1g} of WS_2 were observed at 359.3 and 420.1 cm^{-1}, respectively. The difference of Raman frequencies between these two modes $\Delta\omega$ = 60.8 cm^{-1}, corresponding to a monolayer WS_2 [17]. The Raman spectrum on the SWNT/WS_2 heterostructure shows not only E^1_{2g} and A_{1g} modes of WS_2 but also the G peak of SWNT #1 at 1,592 cm^{-1}. The peak positions of both WS_2 and the SWNT showed no shift on the SWNT/WS_2 heterostrucutre, indicating that no observable strain effect exists between the SWNT and WS_2 [16]. The Raman spectrum of SWNT#1 for 488 nm excitation shows the radial breathing mode (RBM) at 127.8 cm^{-1}, indicating that it is metallic according to the Kataura plot [12].

The corresponding PL mapping image (integrated intensity between 625–635 nm) of this SWNT/WS_2 heterostructure is shown in Fig. 2(a). By comparing to the Raman mapping image in Fig. 1(d), the SWNT #1 can be clearly seen. It is also marked by the white dashed rectangle and the magnified image is shown at the bottom of Fig. 2(a). Figure 2(b) exhibits the PL spectra of WS_2 (green) and SWNT/WS_2 (red), respectively. It has been reported that the PL peak of monolayer WS_2 consists of components from exciton A and trion A^-, which represent the direct transition process at the K point and differ very slightly in energy [18–22]. The fitted curves are shown in the inset, respectively, both showing two components of A and A^-. On monolayer WS_2 without SWNT (green curves), the peak position of the exciton A is at 1.98 eV and that of trion A^- is at 1.95 eV under excitation of 488 nm laser with a power of 0.42 mW. However, on the SWNT/WS_2 heterostructure (red curves), the peak position of the exciton shows a redshift while that of trion does not. The total PL intensity is also enhanced at the SWNT/WS_2 heterostructure. In order to confirm the spectral change along the SWNT, the PL spectra of ten different spots were selected (marked from 1 to 10 in the bottom image of Fig. 2(a)) and plotted in Fig. S3 in the Electronic Supplementary Material (ESM). The spots 1–5 are located on WS_2, which are 400 nm away from SWNT#1, and 6–10 are on the SWNT/WS_2 heterostructure. Figure 2(c) shows the corresponding integrated PL intensities of exciton and trion from the ten spots, and Fig. 2(d) shows the peak positions of exciton and trion, respectively. The increase of intensities of both exciton and trion along the SWNT is clearly seen from Fig. 2(c). However, the intensity ratio between trion and exciton $\frac{I_{A^-}}{I_A}$ is decreased (the right y-axis in Fig. 2(c)). As plotted in Fig. 2(d), the peak position of exciton A was redshifted about 3 meV, while the trion A^- peak position remained almost the same. The right y-axis represents the difference between exciton and trion energies determining the dissociation energy of trion [23, 24]. As a result, the trion dissociation energy is measured to be 34 meV on WS_2 and decreases due to the coupling to SWNT#1.

It has been reported that the decreasing of charge density in MoS_2 resulted in the redshift of excitons and enhanced PL [25]. Apparently, the redshift of exciton peak and the increase of PL intensity observed in our experiments indicate the decrease of charge density at the interface of SWNT/WS_2, and thus the charges transfer from WS_2 to SWNT#1. It has been reported that the intensity of trion is independent on the charge density under the excitation power below 40 μW [24, 25]. In our experiments, the excitation power was up to 0.42 mW, and the contribution of trion to PL could be dominant due to the more excited electrons in the conduction band and be sensitive to the charge density [26–28].

Under chemical and electrical doping of 2D TMD materials, both the ratio $\frac{I_{A^-}}{I_A}$ and trion dissociation energy are related to charge density [24, 25, 29, 30]. The intensity ratio between trion and exciton can be written as [29, 31]

$$\frac{I_{A^-}}{I_A} = \frac{\gamma_{A^-}}{\gamma_A}\left(\frac{\pi\hbar^2 m_{A^-}}{4m_A m_e}\right)\frac{n_e}{k_b T}\exp\left(\frac{E_b}{k_b T}\right) \quad (1)$$

in which γ_{A^-} and γ_A are radiative decay rates of trion and exciton, and m_{A^-} and m_A are effective masses of trion and exciton,

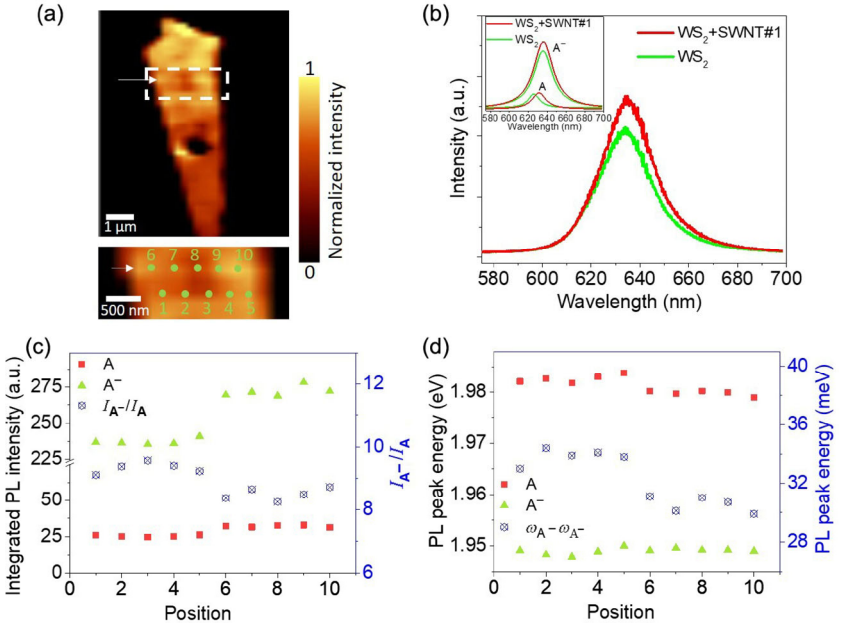

Figure 2 (a) PL mapping of the SWNT#1/WS_2 heterostructure. The bottom image is the magnified area marked by the white dashed rectangle. (b) PL spectra of WS_2 with (red) and without (green) the SWNT#1. The inset gives the corresponding fitting curves composed of exciton and trion, respectively. (c) and (d) The peak intensities and positions of ten PL curves marked in (a) by green spots. The spots 1–5 are located on WS_2 400 nm away from the SWNT. Spots 6–10 are located on the SWNT/WS_2 heterostructure. The blue scatters in (c) represent the intensity ratio of trion and exciton. The blue scatters in (d) are the difference of energy between exciton and trion.

respectively. m_e is the effective mass of electrons, n_e is the charge carrier density and E_b is the binding energy of trion. For limited doping, only n_e is considered as the variable. Thus $\frac{I_{A^-}}{I_A}$ is proportional to the carrier density n_e. Accordingly, the decrease of $\frac{I_{A^-}}{I_A}$ shown in Fig. 2(c) evidenced the decrease of charge density at the interface of SWNT/WS_2. The difference between the peak positions of exciton and trion is [25, 27, 32]

$$\omega_A - \omega_{A^-} = E_b + E_F \quad (2)$$

where ω_A and ω_{A^-} are the PL peak energies of exciton and trion, and E_F is Fermi level of WS_2 that is proportional to n_e, respectively [25, 32]. Therefore, the difference between PL peak energies of exciton and trion is also proportional to n_e. The blue dots in Fig. 2(d) further confirmed that the charge density at the interface of the SWNT/WS_2 was lower than that in pure WS_2.

The charge transfer between WS_2 and SWNT depends on the energy band structure of SWNTs. The heterostructure constructed by monolayer WS_2 and another SWNT (SWNT#2) was also studied. Figure 3(a) shows the Raman mapping image of the G^+ (1,594.5 cm^{-1}) peak of the SWNT#2 in the heterostructure, where the SWNT can be clearly seen. The corresponding Raman spectra of the marked sites in Fig. 3(a) are exhibited in Fig. 3(d). From the Raman spectrum of SWNT#2 (black curve), the RBM peak is observed at 179.6 cm^{-1} and the G peak is split into two Lorentz peaks G^- and G^+. From the G peak and the position of RBM peak, this SWNT can be assigned as a semiconducting one [12, 33]. Similar to that in the SWNT#1/WS_2 heterostructure, no peak shift was observed for both E^1_{2g} and A_{1g} modes of WS_2. Figure 3(b) shows the PL mapping of integrated intensity between 630–640 nm. The dark fringe represents SWNT#2 marked in Fig. 3(a) under WS_2, and it shows that the total PL intensity is weakened at the interface between SWNT#2 and WS_2. Although the slight difference in PL intensity is observable in the mapping image, however, the far-field PL spectra displayed in Fig. 3(e) do not show clear enough difference. Thus, SNOM characterization was performed and the corresponding PL spectra on WS_2 and SWNT/WS_2 were shown at the bottom of Fig. 3(e). A larger spectral difference than that in the far-field can be observed. The corresponding PL mapping of spectral median from the marked area in Fig. 3(b) was shown in Fig. 3(c).

PL spectra of ten spots were chosen from the near-field PL mapping image marked as 1–10 in Fig. 3(c). The corresponding PL spectra are given in Fig. S4 in the ESM. Figures 3(f) and 3(g) display the intensities and peak positions of exciton and trion, respectively. From Fig. 3(f), it is directly observed that exciton is dominant in the PL, which is different from that in Fig. 2(c). This is because the excitation laser power is ~ 30 μW at the aperture of the SNOM tip, much lower than that in the far-field PL mapping of SWNT#1. It has been reported that as the excitation laser power increases, the dominant contribution to PL changes from exciton to trion due to photon-induced electrons doping [27, 28]. The PL intensity of exciton peak is reduced at the interface of SWNT#2/WS_2 while that of trion peak almost remains the same. The blue scatters are the intensity ratio $\frac{I_{A^-}}{I_A}$, which is related to the change of local charge density of WS_2 at the SWNT/WS_2 interface. The increase of $\frac{I_{A^-}}{I_A}$ indicates that the local charge density is increased due to the contact with SWNT#2, and thus the charges transfer from the SWNT to WS_2. It can be seen in Fig. 3(f) that the PL peak of exciton in the heterostructure blue-shifts by about 1 meV, while that of trion is red-shifted by about 1 meV. The peak shifts further confirm that the local charge density in WS_2 in the 1D/2D heterostructure is higher than that in pure WS_2 [24, 25, 29]. Table S1 in the ESM gives the average values of PL peak energy and intensity of the selected spectra from both the SWNT#1/WS_2 and SWNT#2/WS_2 heterostructures.

Figure 4(a) shows the diagram of charge transfer process in the heterostructures based on the above experimental results. It has been reported that pristine monolayer WS_2 on SiO_2 substrate is n-doped [27, 30, 34]. The energy band diagrams of nanotubes schematically represent the chosen SWNT#1 of metallic type and SWNT#2 of semiconducting type [35, 36]. For the SWNT#1/WS_2, the Fermi level of the nanotube is lower than that of WS_2, so that the charge transfer occurs from WS_2

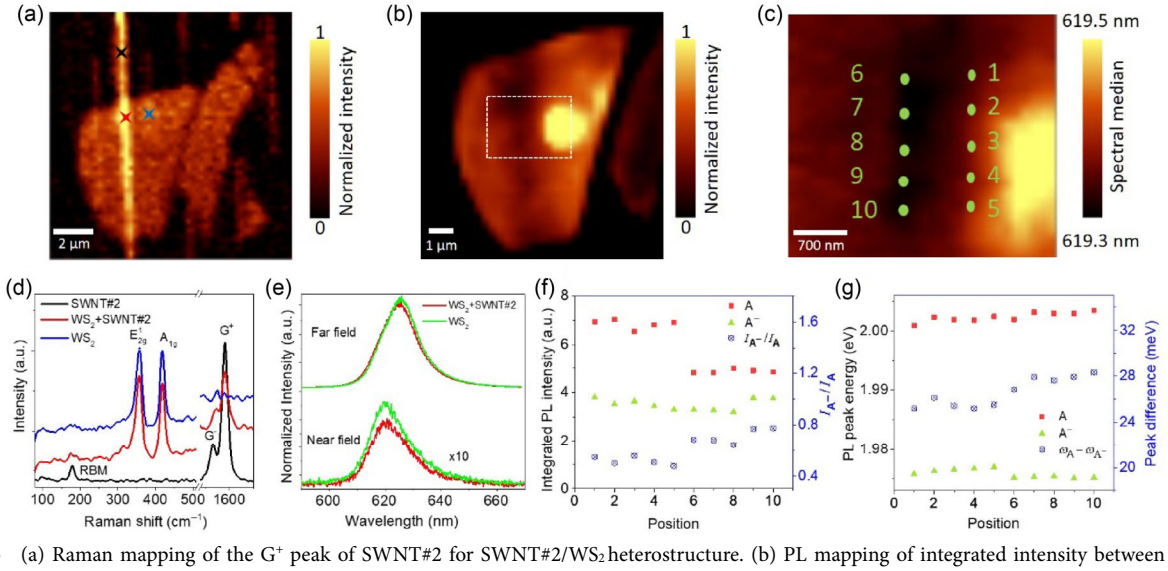

Figure 3 (a) Raman mapping of the G^+ peak of SWNT#2 for SWNT#2/WS_2 heterostructure. (b) PL mapping of integrated intensity between 630 and 640 nm. (c) Near-field mapping of spectral median of the zone marked in (b) by the white dotted box. (d) The Raman spectra chosen from three sites marked in (a). (e) PL spectra of WS_2 with (red) and without (green) SWNT#2 obtained from ((b), far-field) and ((c), near-field), respectively. (f) and (g) The peak intensities (f) and positions (g) of ten PL spectra from (c). The blue scatters in (f) represent the intensity ratio of trion and exciton, and in (g) represent the peak energy difference between exciton and trion.

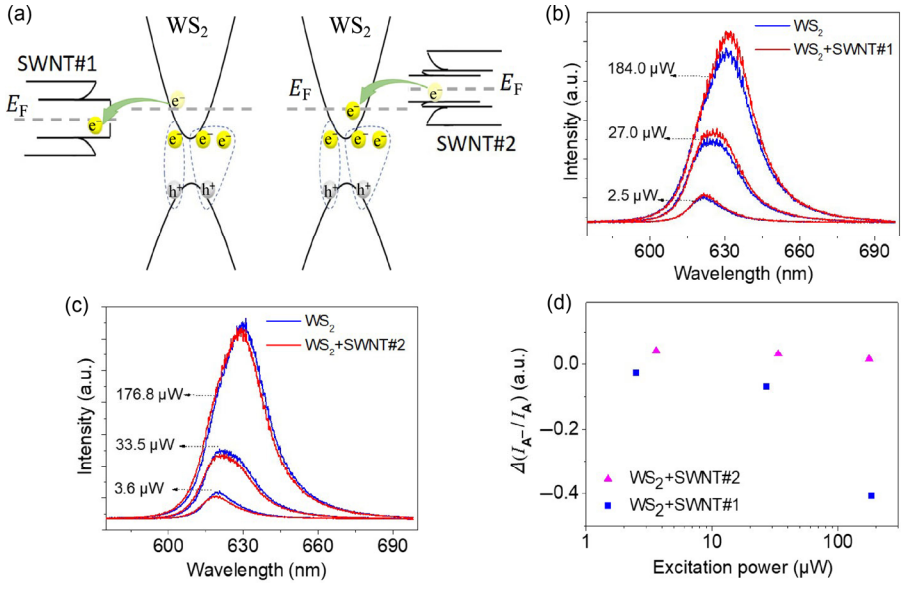

Figure 4 (a) The scheme of the opposite charge transfer processes in the different SWNT/WS_2 heterostructures. (b) and (c) Excitation power dependent PL spectra from SWNT#1/WS_2 (b) and SWNT#2/WS_2 (c). Red curves were from heterostructures and blue curves were from monolayer WS_2. (d) The different PL intensity ratio of trion and exciton as a function of laser power.

to the carbon nanotube and the local charge density of WS_2 at the interface decreases. This process causes the decrease of energy difference between exciton and trion and the decrease of intensity ratio $\frac{I_{A^-}}{I_A}$. Instead, the charge transfer occurs from SWNT#2 to monolayer WS_2, which causes the local charge density to increase in WS_2 for the SWNT/WS_2 heterostructure. This process enhances the formation rate of trion and lowers the relative intensity of exciton. The energy difference between exciton and trion is increased at the same time.

The excitation laser power dependent PL spectra were measured on the two heterostructures in order to further confirm the charge transfer. As shown in Figs. 4(b) and 4(c), when the excitation power increased from 2.5 to 184 μW, the total PL intensity increased and the main contribution to the PL changed from excitons to trions. This can be explained by the increased photon-induced carriers that facilitate the formation of trions [16, 32, 37]. The increase of photon-induced carriers also leads to the lifting of the quasi-Fermi level of WS_2 [23, 38]. Therefore, the energy difference between WS_2 and SWNT#1 is increased and that between WS_2 and SWNT#2 is decreased. The difference of charge density between SWNT/WS_2 heterostructure and WS_2 is related to the difference of $\frac{I_{A^-}}{I_A}$ measured for WS_2, defined as $\Delta\left(\frac{I_{A^-}}{I_A}\right)=\left(\frac{I_{A^-}}{I_A}\right)_{\mathrm{SWNT/WS_2}}-\left(\frac{I_{A^-}}{I_A}\right)_{\mathrm{WS_2}}$. Figure 4(d) shows the dependence of $\Delta\left(\frac{I_{A^-}}{I_A}\right)$ for the two SWNT/WS_2 heterostructures to the excitation power. For SWNT#1/WS_2, $\Delta\left(\frac{I_{A^-}}{I_A}\right)$ is always negative, meaning that $\frac{I_{A^-}}{I_A}$ for the SWNT#1/WS_2 heterotructure is smaller than that on pure WS_2, and the relative contribution of trions is decreased due to the coupling to SWNT. With increasing laser power from 2.5 to 184 μW, $\Delta\left(\frac{I_{A^-}}{I_A}\right)$ changes from −0.026 to −0.407. The further decreasing of $\Delta\left(\frac{I_{A^-}}{I_A}\right)$ indicates the increased charge transfer from WS_2 to SWNT#1 at higher laser power. While for SWNT#2/WS_2, $\Delta\left(\frac{I_{A^-}}{I_A}\right)$ is positive, meaning that the relative contribution of trions is increased due to the coupling to SWNT#2, and the charge transfer occurs from SWNT#2 to WS_2. With increasing laser power from 3.6 to 176.8 μW, it decreases slightly from 0.042 to 0.016, indicating a decreased charge transfer from SWNT#2 to WS_2 at higher laser power. It should be noted that for a different SWNT, the charge transfer and the modulation of excitons and trions depend on the energy band alignment between the SWNT and WS_2.

4 Conclusion

In summary, we studied mixed dimensional vdW heterostructures consisting of monolayer WS_2 and individual SWNTs, and observed different modulation of excitons and trions between two SWNT/WS_2 heterostructures. For the SWNT#1/WS_2 heterostructure, PL of WS_2 was enhanced and the peak of exciton got red-shifted, while for the SWNT#2/WS_2 heterostructure, the peak of exciton in WS_2 was blue-shifted and the PL intensity was weakened. These contrary phenomena in the two heterostructures are the consequence of opposite charge transfer directions occurred at the interface of SWNT/WS_2 heterostructures. The excitation power dependent PL spectra further demonstrated the different charge transfer processes between SWNTs and WS_2. Our results revealed the charge transfer and tunable excitonic behavior of SWNT/WS_2 mixed dimensional vdW heterostructures, and can be useful for future optoelectronic applications based on 1D/2D mixed dimensional vdW heterostructures.

Acknowledgements

This work was financially supported by the National Basic Research Program of China (Nos. 2018YFA0703502 and 2016YFA0200104) and the National Natural Science Foundation of China (Nos. 51720105003, 21790052, 21573004 and 21974004).

Electronic Supplementary Material: Supplementary material (experiment details) is available in the online version of this article at https://doi.org/10.1007/s12274-020-2895-5.

References

[1] Sun, Y.; Zhong, W.; Wang, Y. Q.; Xu, X. B.; Wang, T. T.; Wu, L. Q.; Du, Y. W. MoS_2-based mixed-dimensional van der Waals heterostructures: A new platform for excellent and controllable microwave-absorption performance. *ACS Appl. Mater. Interfaces* **2017**, *9*, 34243–34255.

[2] Jariwala, D.; Sangwan, V. K.; Wu, C. C.; Prabhumirashi, P. L.; Geier, M. L.; Marks, T. J.; Lauhon, L. J.; Hersam, M. C. Gate-tunable carbon nanotube-MoS_2 heterojunction p-n diode. *Proc. Natl. Acad. Sci. USA* **2013**, *110*, 18076–18080.

[3] Novoselov, K. S.; Mishchenko, A.; Carvalho, A.; Castro Neto, A. H. 2D materials and van der Waals heterostructures. *Science* **2016**, *353*, aac9439.

[4] Tian, H.; Chin, M. L.; Najmaei, S.; Guo, Q. S.; Xia, F. N.; Wang, H.; Dubey, M. Optoelectronic devices based on two-dimensional transition metal dichalcogenides. *Nano Res.* **2016**, *9*, 1543–1560.

[5] Jariwala, D.; Marks, T. J.; Hersam, M. C. Mixed-dimensional van der Waals heterostructures. *Nat. Mater.* **2017**, *16*, 170–181.

[6] Wu, H. L.; Si, H. N.; Zhang, Z. H.; Kang, Z.; Wu, P. W.; Zhou, L. X.; Zhang, S. C.; Zhang, Z.; Liao, Q. L.; Zhang, Y. All-inorganic perovskite quantum dot-monolayer MoS_2 mixed-dimensional van der Waals heterostructure for ultrasensitive photodetector. *Adv. Sci.* **2018**, *5*, 1801219.

[7] Sun, Y.; Xu, J. L.; Qiao, W.; Xu, X. B.; Zhang, W. L.; Zhang, K. Y.; Zhang, X.; Chen, X.; Zhong, W.; Du, Y. W. Constructing two-, zero-, and one-dimensional integrated nanostructures: An effective strategy for high microwave absorption performance. *ACS Appl. Mater. Interfaces* **2016**, *8*, 31878–31886.

[8] Shang, H. M.; Chen, H. Y.; Dai, M. L.; Hu, Y. X.; Gao, F.; Yang, H. H.; Xu, B.; Zhang, S. C.; Tan, B. Y.; Zhang, X. et al. A mixed-dimensional 1D Se–2D InSe van der Waals heterojunction for high responsivity self-powered photodetectors. *Nanoscale Horiz.* **2020**, *5*, 564–572.

[9] Qin, J. K.; Yan, H.; Qiu, G.; Si, M. W.; Miao, P.; Duan, Y. Q.; Shao, W. Z.; Zhen, L.; Xu, C. Y.; Ye, P. D. Hybrid dual-channel phototransistor based on 1D t-Se and 2D ReS_2 mixed-dimensional heterostructures. *Nano Res.* **2019**, *12*, 669–674.

[10] Henning, A.; Sangwan, V. K.; Bergeron, H.; Balla, I.; Sun, Z. Y.; Hersam, M. C.; Lauhon, L. J. Charge separation at mixed-dimensional single and multilayer MoS_2/silicon nanowire heterojunctions. *ACS Appl. Mater. Interfaces* **2018**, *10*, 16760–16767.

[11] Park, S.; Vosguerichian, M.; Bao, Z. A. A review of fabrication and applications of carbon nanotube film-based flexible electronics. *Nanoscale* **2013**, *5*, 1727–1752.

[12] Weisman, R. B.; Bachilo, S. M. Dependence of optical transition energies on structure for single-walled carbon nanotubes in aqueous suspension: An empirical Kataura plot. *Nano Lett.* **2003**, *3*, 1235–1238.

[13] Liu, Y. D.; Wang, F. Q.; Wang, X. M.; Wang, X. Z.; Flahaut, E.; Liu, X. L.; Li, Y.; Wang, X. R.; Xu, Y. B.; Shi, Y. et al. Planar carbon nanotube-graphene hybrid films for high-performance broadband photodetectors. *Nat. Commun.* **2015**, *6*, 8589.

[14] Zhang, K.; Wei, Y.; Zhang, J.; Ma, H.; Yang, X. H.; Lu, G. T.; Zhang, K. N.; Li, Q. Q.; Jiang, K. L.; Fan, S. S. Electrical control of spatial resolution in mixed-dimensional heterostructured photodetectors. *Proc. Natl. Acad. Sci. USA* **2019**, *116*, 6586–6593.

[15] Liu, C.; Hong, H.; Wang, Q. H.; Liu, P.; Zuo, Y. G.; Liang, J.; Cheng, Y.; Zhou, X.; Wang, J. H.; Zhao, Y. et al. Strong-coupled hybrid structure of carbon nanotube and MoS_2 monolayer with ultrafast interfacial charge transfer. *Nanoscale* **2019**, *11*, 17195–17200.

[16] Plechinger, G.; Nagler, P.; Kraus, J.; Paradiso, N.; Strunk, C.; Schüller, C.; Korn, T. Identification of excitons, trions and biexcitons in single-layer WS_2. *Phys. Status Solidi-Rapid Res. Lett.* **2015**, *9*, 457–461.

[17] Berkdemir, A.; Gutiérrez, H. R.; Botello-Méndez, A. R.; Perea-López, N.; Elías, A. L.; Chia, C. I.; Wang, B.; Crespi, V. H.; López-Urías, F.; Charlier, J. C. et al. Identification of individual and few layers of WS_2 using Raman spectroscopy. *Sci. Rep.* **2013**, *3*, 1755.

[18] Hill, H. M.; Rigosi, A. F.; Roquelet, C.; Chernikov, A.; Berkelbach, T. C.; Reichman, D. R.; Hybertsen, M. S.; Brus, L. E.; Heinz, T. F. Observation of excitonic Rydberg states in monolayer MoS_2 and WS_2 by photoluminescence excitation spectroscopy. *Nano Lett.* **2015**, *15*, 2992–2997.

[19] Shi, H. L.; Pan, H.; Zhang, Y. W.; Yakobson, B. I. Quasiparticle band structures and optical properties of strained monolayer MoS_2 and WS_2. *Phys. Rev. B* **2013**, *87*, 155304.

[20] Zhu, B. R.; Chen, X.; Cui, X. D. Exciton binding energy of monolayer WS_2. *Sci. Rep.* **2015**, *5*, 9218.

[21] Shang, J. Z.; Shen, X. N.; Cong, C. X.; Peimyoo, N.; Cao, B. C.; Eginligil, M.; Yu, T. Observation of excitonic fine structure in a 2D transition-metal dichalcogenide semiconductor. *ACS Nano* **2015**, *9*, 647–655.

[22] Chernikov, A.; Berkelbach, T. C.; Hill, H. M.; Rigosi, A.; Li, Y. L.; Aslan, O. B.; Reichman, D. R.; Hybertsen, M. S.; Heinz, T. F. Exciton binding energy and nonhydrogenic Rydberg series in monolayer WS_2. *Phys. Rev. Lett.* **2014**, *113*, 076802.

[23] Mitioglu, A. A.; Plochocka, P.; Jadczak, J. N.; Escoffier, W.; Rikken, G. L. J. A.; Kulyuk, L.; Maude, D. K. Optical manipulation of the exciton charge state in single-layer tungsten disulfide. *Phys. Rev. B* **2013**, *88*, 245403.

[24] Peimyoo, N.; Yang, W. H.; Shang, J. Z.; Shen, X. N.; Wang, Y. L.; Yu, T. Chemically driven tunable light emission of charged and neutral excitons in monolayer WS_2. *ACS Nano* **2014**, *8*, 11320–11329.

[25] Mak, K. F.; He, K. L.; Lee, C.; Lee, G. H.; Hone, J.; Heinz, T. F.; Shan, J. Tightly bound trions in monolayer MoS_2. *Nat. Mater.* **2013**, *12*, 207–211.

[26] Ko, P. J.; Abderrahmane, A.; Thu, T. V.; Ortega, D.; Takamura, T.; Sandhu, A. Laser power dependent optical properties of mono- and few-layer MoS_2. *J. Nanosci. Nanotechnol.* **2015**, *15*, 6843–6846.

[27] McCreary, K. M.; Hanbicki, A. T.; Singh, S.; Kawakami, R. K.; Jernigan, G. G.; Ishigami, M.; Ng, A.; Brintlinger, T. H.; Stroud, R. M.; Jonker, B. T. The effect of preparation conditions on Raman and photoluminescence of monolayer WS_2. *Sci. Rep.* **2016**, *6*, 35154.

[28] Wang, X. H.; Ning, J. Q.; Su, Z. C.; Zheng, C. C.; Zhu, B. R.; Xie, L.; Wu, H. S.; Xu, S. J. Photoinduced doping and photoluminescence signature in an exfoliated WS_2 monolayer semiconductor. *RSC Adv.* **2016**, *6*, 27677–27681.

[29] Mouri, S.; Miyauchi, Y.; Matsuda, K. Tunable photoluminescence of monolayer MoS_2 via chemical doping. *Nano Lett.* **2013**, *13*, 5944–5948.

[30] Ross, J. S.; Wu, S. F.; Yu, H. Y.; Ghimire, N. J.; Jones, A. M.; Aivazian, G.; Yan, J. Q.; Mandrus, D. G.; Xiao, D.; Yao, W. et al. Electrical control of neutral and charged excitons in a monolayer semiconductor. *Nat. Commun.* **2013**, *4*, 1474.

[31] Schmidt, T.; Lischka, K.; Zulehner, W. Excitation-power dependence of the near-band-edge photoluminescence of semiconductors. *Phys. Rev. B* **1992**, *45*, 8989–8994.

[32] Huard, V.; Cox, R. T.; Saminadayar, K.; Arnoult, A.; Tatarenko, S. Bound states in optical absorption of semiconductor quantum wells containing a two-dimensional electron gas. *Phys. Rev. Lett.* **2000**, *84*, 187–190.

[33] Dresselhaus, M. S.; Dresselhaus, G.; Saito, R.; Jorio, A. Raman spectroscopy of carbon nanotubes. *Phys. Rep.* **2005**, *409*, 47–99.

[34] Dolui, K.; Rungger, I.; Sanvito, S. Origin of the n-type and p-type conductivity of MoS_2 monolayers on a SiO_2 substrate. *Phys. Rev. B* **2013**, *87*, 165402.

[35] Cabria, I.; Mintmire, J. W.; White, C. T. Metallic and semiconducting narrow carbon nanotubes. *Phys. Rev. B* **2003**, *67*, 121406(R).

[36] Itkis, M. E.; Niyogi, S.; Meng, M. E.; Hamon, M. A.; Hu, H.; Haddon, R. C. Spectroscopic study of the Fermi level electronic structure of single-walled carbon nanotubes. *Nano Lett.* **2002**, *2*, 155–159.

[37] Finkelstein, G.; Shtrikman, H.; Bar-Joseph, I. I. Optical spectroscopy of a two-dimensional electron gas near the metal-insulator transition. *Phys. Rev. Lett.* **1995**, *74*, 976–979.

[38] Currie, M.; Hanbicki, A. T.; Kioseoglou, G.; Jonker, B. T. Optical control of charged exciton states in tungsten disulfide. *Appl. Phys. Lett.* **2015**, *106*, 201907.